Electronic correlation-driven exotic quantum phase transitions in infinite-layer manganese oxide

Heng Jin,[1,2] Xiaojun Chen,[3,4] Liang Qiao,[4] and Bing Huang[2,1,*]
[1]*Department of Physics, Beijing Normal University, Beijing 100875, China*
[2]*Beijing Computational Science Research Center, Beijing 100193, China*
[3]*School of Mechanical Engineering, Chengdu University, Chengdu 610106, China*
[4]*School of Physics, University of Electronic Science and Technology of China, Chengdu 610106, China*

(Received 19 April 2023; accepted 17 August 2023; published 30 August 2023)

Despite the intensive interest in copper- and nickel-based superconductivity in infinite-layer structures, the physical properties of many other infinite-layer transition-metal oxides remain largely unknown. Here we unveil, by the first-principles calculations, the electronic correlation (EC)-driven series of quantum-phase transitions (QPTs) in infinite-layer $SrMnO_2$, where spin and charge orders are strongly interwoven. At a weak EC region, $SrMnO_2$ is a ferromagnetic metal with anisotropic spin transportation, as a promising spin valve under room temperature. When EC is slightly increased, a structural transition accompanied by charge/bond disproportion occurs as a consequence of Fermi surface nesting, resulting in a ferromagnetic insulator with reduced Curie temperature. When EC is further enhanced, another structural transition occurs that drives the system into a different-type multiferroic phase with piezoelectricity-tunable antiferromagnetic orders. Therefore, infinite-layer $SrMnO_2$ is possibly a unique system on the quantum critical point, where small perturbations of EC can realize a series of QPTs.

DOI: 10.1103/PhysRevB.108.054106

I. INTRODUCTION

Many fascinating phenomena in condensed matter physics, including magnetism, ferroelectricity, colossal magnetoresistance, quantum Hall effect, superconductivity, and charge/orbital/spin order [1–8], are observed in transition metal oxides (TMOs) with a typical formula of ABO_3. With decades of effort, the synthesis of TMOs becomes mature and efficient [9,10], which provides new opportunities to generate artificial oxides by chemical doping, alloying, or topotactic reduction. The special interest in reduction reaction arises from the discovery of copper-based superconductivity in the infinite-layer phase [11,12] and is accelerated by nickel-based superconductivity with a similar structure [13]. In general, an infinite-layer TMO with a formula of ABO_2 consists of a quasi-2D BO_2 plane separated by an A-dominated charge-reservoir spacer layer, whose physical properties are strongly influenced by different crystal-field splitting and a large shift of Fermi level due to the escape of apical oxygen from ABO_3. Accompanied by the synthesis and characterization of infinite-layer ABO_2 with $B =$ Cu (e.g., $CaCuO_2$ [11,12]), Ni (e.g., $NdNiO_2$ [13]), Fe (e.g., $SrFeO_2$ [14,15]), and Co (e.g., $CaCoO_2$ [16]), an interesting question arises: as the neighbor of existing ABO_2 in the element periodic table, can $AMnO_2$ exhibit new physics different from the existing ABO_2? While experimental synthesis of $AMnO_2$ may be time consuming, theoretical predictions play an important role in identifying their fascinating properties in advance, guiding future experimental measurements.

Electronic correlation (EC) is indispensable in understanding charge/spin order, non-Fermi-liquid behavior, Mott insulator, and unconventional superconductivity [17,18]. The EC is usually strong in systems containing open d or f shells because of narrow bandwidth and highly degenerate atomic orbitals. The simplest model to describe the EC effect is the Hubbard model, $H = -\sum_{\langle i,j\rangle} t_{ij}(c^{\dagger}_{i\sigma}c_{j\sigma} + c^{\dagger}_{j\sigma}c_{i\sigma}) + U\sum_i n_{i\uparrow}n_{i\downarrow}$, where i and j are sites and σ denotes spin and U represents the strength of EC, giving a successful interpretation of the correlation-driven Mott phase transition. Density functional theory (DFT) flavors of this model [19–21] could give a good description of the ground-state structures and electronic structures on the mean-field level as precursors for many-body phenomena. For example, the antiferromagnetic (AFM) order in $SrFeO_2$ [22], geometric frustration in $CaCoO_2$ [16], and self-doping effect in $NdNiO_2$ [23] can be well understood by the DFT $+ U$ calculations. Remarkably, the mentioned physical properties of ABO_2 ($B =$ Fe, Co, and Ni) are insensitive to the small change of U.

In this study, we unveil, by the first-principles calculations, the EC-driven continuous quantum-phase transitions in infinite-layer $SrMnO_2$, where spin and charge orders are strongly interwoven. At a small EC region, $SrMnO_2$ is a ferromagnetic metal with anisotropic spin transportation. When the EC is slightly enhanced, a structural transition accompanied by charge/bond disproportion occurs due to Fermi surface nesting (FSN), resulting in a ferromagnetic insulator. With the further enhancement of EC, a structural transition occurs that can transform the system into degenerately AFM insulators with tunable magnetic order by the piezoelectric response, resulting in a different type of multiferroics. Our study

*Corresponding author: bing.huang@csrc.ac.cn

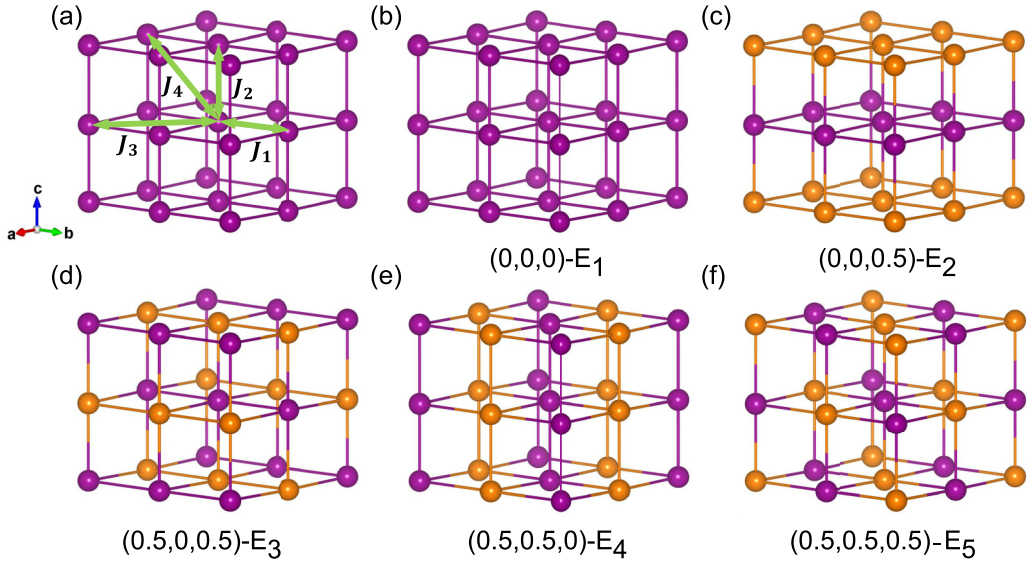

FIG. 1. Magnetic configurations of $SrMnO_2$ considered in this study. (a) Definition of exchange parameter $J_i (i = 1, 2, 3, 4)$ in the Heisenberg model. (b) Ferromagnetic and (c)–(f) antiferromagnetic configurations. For simplicity, only Mn atoms are shown and different spins are colored with purple and orange respectively.

demonstrates that infinite-layer $SrMnO_2$ is possibly a good system with tunable quantum phase transitions.

II. METHODS

DFT calculations. Our first-principles calculations are performed with the Vienna *ab initio* simulation package (VASP) [24] with projector augmented wave method (PAW) [25]. The exchange-correlation term is treated with the Perdew-Burke-Ernzerhof (PBE) [26] form of the generalized gradient approximation. The $4s^2 4p^6 5s^2$, $3p^6 4s^1 3d^6$ and $2s^2 2p^4$ electrons are treated as valence electrons for Sr, Mn, and O, respectively. Gaussian smearing of 0.05 eV has been adopted in our calculations. We study the correlation effect within the scheme of LSDA + U with the flavor of Dudarev's form [21]. Since $SrMnO_2$ has not been synthesized experimentally, it is hard to accurately determine how large U is supposed to be. Insight can be found based on the fact that for $SrMnO_3$ typically $U = 1.7$–3.0 eV can give the best fitting to experiments [27,28]. Hence, we safely regard U in $SrMnO_2$ as a parameter in the range 1–5 eV. We start geometric optimization with a $2\times2\times2$ supercell [including eight formula units (f.u.)] to accommodate possible structural distortions and magnetic configurations (see details in Fig. 1). We use energy cutoff of 520 eV and k mesh of $4\times4\times5$ over the Brillouin zone until the energy difference of iteration is smaller than 10^{-6} eV. And for static calculations, a denser k mesh of $8\times8\times9$ and convergence criterion of the total energy of 10^{-7} eV are used. Our test calculations confirm that the spin-orbital coupling (SOC) effect, which is not included in our following study except for the calculation of magnetocrystalline anisotropic energy, will not influence our main conclusion. The Fermi surface is shown with FERMISURFER software [29] and the unfolded band structure is calculated with the BANDUP code [30,31]. The phonon spectra are calculated based on a $2\times2\times2$ supercell with density functional perturbation theory (DFPT), as implemented in PHONOPY software [32], with precision consistent with the geometry relaxation. The piezoelectricity is calculated with the DFPT method. We use MCSOLVER software [33] for classic Monte Carlo (MC) simulation for a $12\times12\times12$ supercell to solve the Heisenberg model and to obtain the Curie temperature. To determine the critical temperature of the charge order, we perform *ab initio* molecular dynamic (AIMD) with NVT ensembles and a Nose-Hoover thermostat [34,35] considering a supercell containing 64 f.u. and up to 3.6 ps. The evaluation of U from first-principles calculations are performed with DFPT [36,37], as implemented in QUANTUM ESPRESSO (QE) software [38].

Heisenberg model. To determine the Curie temperature, the Heisenberg model is used to construct MC simulation parameters. The classic spin Hamiltonian is $H = \sum_{\langle ij \rangle} J_{ij} \vec{S}_i \cdot \vec{S}_j + \sum_i D S_{iz}^2$, where J_{ij} is the exchange parameter and D is the spin anisotropy parameter.J_{ij} can be obtained by mapping the total energy of different magnetic configurations to the model. The atomic position is fixed to the ferromagnetic one, as in the static calculations. We have

$$E_1 = E_0 + S^2(2J_1 + J_2 + 2J_3 + 4J_4), \quad (1)$$

$$E_2 = E_0 + S^2(2J_1 - J_2 + 2J_3 - 4J_4), \quad (2)$$

$$E_3 = E_0 + S^2(-J_2 - 2J_3), \quad (3)$$

$$E_4 = E_0 + S^2(-2J_1 + J_2 + 2J_3 - 4J_4), \quad (4)$$

$$E_5 = E_0 + S^2(-2J_1 - J_2 + 2J_3 + 4J_4), \quad (5)$$

where the definition of J_i $(i = 1, 2, 3, 4)$ is showed in Fig. 1. E_0 is the energy of primitive cells unrelated to spin configuration. Here, based on the total magnetic moments, we approximate $S^2 = 4$. By solving the equations, the exchange parameter J_i $(i = 1, 2, 3, 4)$ is obtained, as shown in Table I.

TABLE I. Exchange parameters obtained by DFT energy mapping of different AFM configurations. Here negative D represents spin parallel to c. The unit is meV.

	J_1	J_2	J_3	J_4	D
$P4/mmm$ ($U = 1$ eV)	−5.38	−17.67	1.97	−0.34	−0.10
$CmCm$ ($U = 3$ eV)	−1.82	−9.15	0.28	0.17	−0.10

III. RESULTS AND DISCUSSION

Continuous structural transitions induced by EC. In the topotactic reduction process, the apical O atoms are removed from the perovskite $SrMnO_3$ structure, accompanied by the reduction of the space group from $Pm\bar{3}m$ to $P4/mmm$. As shown in Fig. 2(a), the $SrMnO_2$ structure is characterized by stacking the Mn-O plane and interstitial Sr atom along the c axis. We have evaluated the ground-state transition as a function of U. Specifically, one ferromagnetic (FM) [(0,0,0)] and four AFM [(0,0,0.5), (0.5,0,0.5), (0.5,0.5,0), and (0.5,0.5,0.5)] orders are considered (Fig. 1). As shown in Fig. 2(d), the $P4/mmm$ phase is only stable with small U (∼1 eV), being a FM metal. Unexpectedly, when U is increased to 2–3 eV, additional movements of O atoms can be found [Fig. 2(b)] to reach a different ground-state configuration. Four O atoms move toward central Mn and away from nearest-neighbor Mn within the Mn-O plane, forming a frozen breathing mode in layer 1 and antiphase modulation in the neighboring Mn-O plane (layer 2). Therefore, the structure is reconstructed with $CmCm$ space group and contains a $2\times2\times2$ f.u. in the primitive cell, with obvious charge/bond disproportion order. When U is further increased to 4–5 eV, the ground-state configuration of $SrMnO_2$ is featured by a bent Mn-O plane, rotation of Mn-O tetrahedrons, and displacement of Sr along the c axis [Fig. 2(c)]. This structure has a space group of $P\bar{4}2_1m$, including $\sqrt{2}\times\sqrt{2}\times2$ f.u. in the primitive cell. Interestingly, the two lowest-energy (0.5,0.5,0) and (0.5,0.5,0.5) AFM configurations are nearly degenerate with an energy difference <1 meV/f.u., despite both being insulators.

Anisotropic spin valve. When $U = 1$ eV, the ground state of $SrMnO_2$ is a FM metal. The band structures of both spin channels are shown in Figs. 3(a) and 3(b). The band splitting due to Stoner instability is ∼4.25 eV, creating dramatically different electronic states in different spin channels around E_F. In the spin ↑ channel, $d_{x^2-y^2}$ contributes mainly to the band across E_F. Thus, the Fermi surface behaves as a strong quasi-2D feature and the electron density around E_F shows clear in-plane distribution with high Fermi velocity in the 2D Mn-O plane [Fig. 3(c)]. Overall, the band structure of the spin ↑ channel highly resembles infinite-layer nickelates and cuprates [39]. Remarkably, the unoccupied band close to E_F at A is attributed to an interstitial electron (Fig. 4), which is occupied in $NdNiO_2$ and influences superconductivity fundamentally [40]. The band structure of the spin ↓ channel shows a very different feature [Fig. 3(b)]. All Mn d orbitals are all pushed above E_F except half occupied d_{z^2}. The sharp band dispersion along Γ-Z crossing E_F is observed, enabling the Fermi surface of the spin ↓ channel to be quasi-1D with high Fermi velocity along Γ-Z [Fig. 3(d)]. Therefore, the electron density around E_F shows conducting behavior along the c direction.

From MC simulation, the Curie temperature T_C estimated by the peak of specific heat is predicted to be ∼427 K [Fig. 3(e)], far above room temperature. These unique features of the Fermi surface of $SrMnO_2$ are highly desirable for designing a spin valve. Common FM metal is conductive for the transportation of both spin currents from any direction while half metal allows transportation of one spin current and prohibits transportation of opposite spin from any direction [41]. In $SrMnO_2$, the transport of spin current is anisotropic. As shown in Fig. 3(f), the transport behavior depends on the direction of spin flows. If electrons are injected along the a-b plane, spin ↓ electrons will be filtered out; if the electrons are injected along the c direction, spin ↑ electrons will be filtered out. Thus, the spin-polarized current

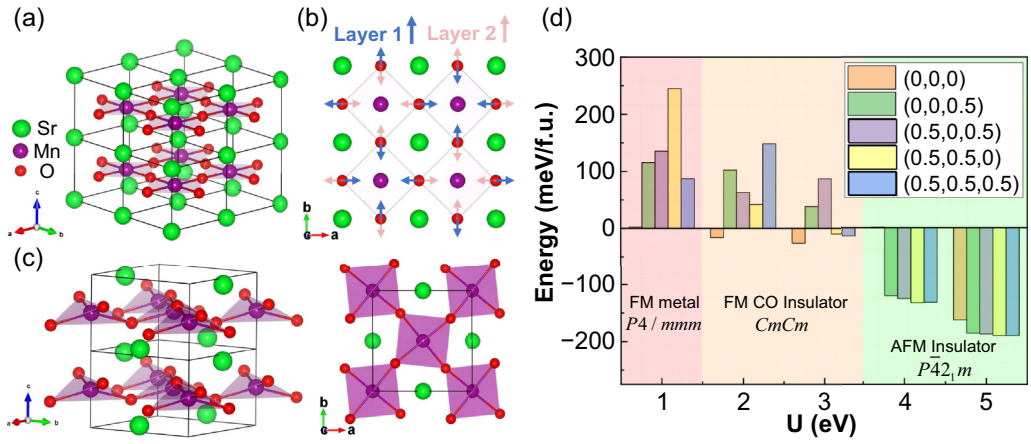

FIG. 2. Structural evolution of $SrMnO_2$ with U. (a) Infinite-layer $SrMnO_2$ with $P4/mmm$ symmetry. The Mn-O plane is illustrated with shadowed squares. (b) Schematic diagram of frozen breathing mode in charge/bond disproportion state of $SrMnO_2$ with $CmCm$ symmetry. Arrows with different colors indicate the movement of oxygens in different Mn-O layers (denoted as Layer 1 and Layer 2). (c) Side view (left) and top view (right) of $SrMnO_2$ with $P\bar{4}2_1m$ symmetry. (d) Total energy versus U of geometrically relaxed $SrMnO_2$ within a $2\times2\times2$ supercell under different magnetic configurations. The energy of FM $P4/mmm$ phase is set to zero. CO: charge order.

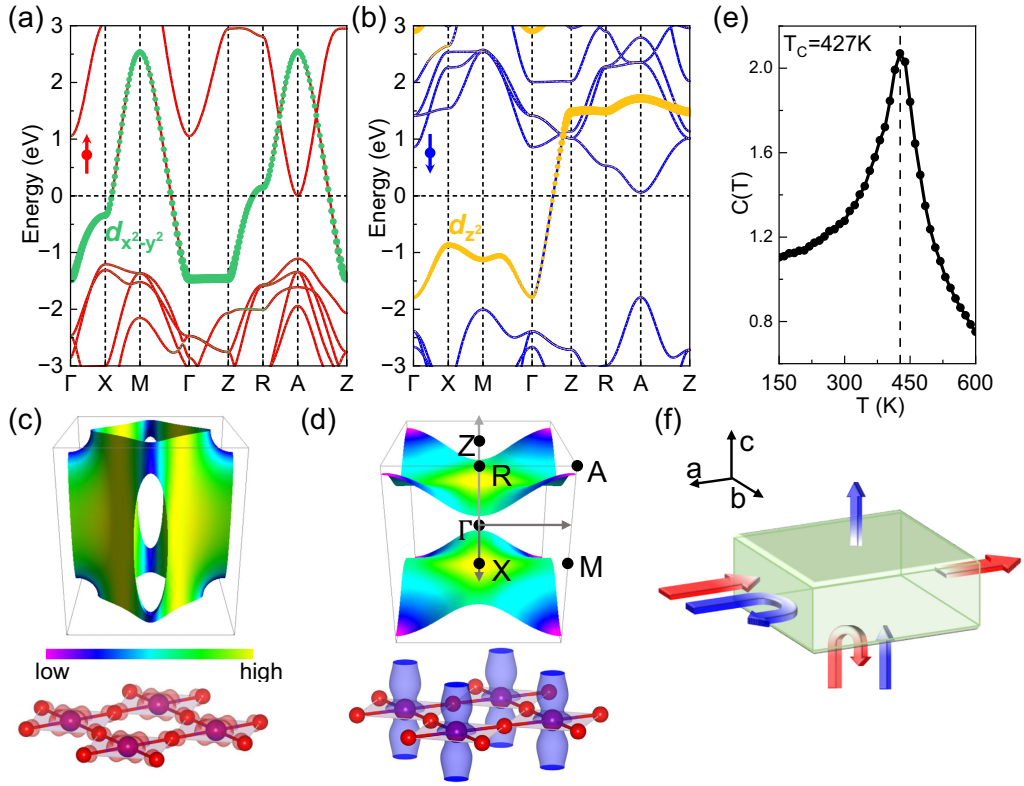

FIG. 3. Electronic properties of ferromagnetic $P4/mmm$ phase with $U = 1$ eV. Band structures of (a) spin ↑ and (b) spin ↓ channels. Orbital projections are illustrated with color dots. Fermi level (E_F) is set to zero. Fermi surface in Brillioun zone (up panel) and spin-resolved electron density distribution summed over $E_F \pm 0.1$ eV (down panel) for (c) spin ↑ and (d) spin ↓ band structures. Fermi velocity is illustrated with the color bar and the electron density isosurface is set to 2×10^{-3} $e/Å^3$. (e) MC-simulated specific heat $C(T)$ versus temperature based on the Heisenberg model. (f) Diagram of the anisotropic spin valve. Spin ↑ and spin ↓ currents are illustrated with red and blue, respectively.

can be obtained merely by changing the direction of injected electrons.

Emergent charge/bond disproportion order. As shown in Fig. 2(d), when U is increased to 2–3 eV, the ground state is accompanied by charge/bond disproportion. This can be indicated by the phonon spectra of the FM $P4/mmm$ phase [Fig. 5(a)], which show dramatic instabilities only when $U =$ 3 eV. For these two unstable modes, the major imaginary mode reaching $-6i$ THz at A is indeed a breathing mode involving the vibration of Mn-O bonds, as depicted in Fig. 2(b). In the charge/bond disproportion order phase [Fig. 5(b)], two kinds of Mn-O bonds are obtained (2.09 and 1.95 Å), resulting in two kinds of Mn atoms ($\mu_{Mn1} = 4.3\mu_B$ and $\mu_{Mn2} = 3.4\mu_B$). To unveil the change of electronic states as a consequence of the formation of charge order, the unfolded band structures are plotted and compared with undistorted ones [Figs. 5(c) and 5(d)]. Overall, the formation of charge order opens energy gaps in both spin channels, resulting in a FM insulating phase. Specifically, the local gap of the spin ↑ channel is about ∼1 eV while in the spin ↓ channel only a gap of ∼0.5 eV along Γ-Z can be found.

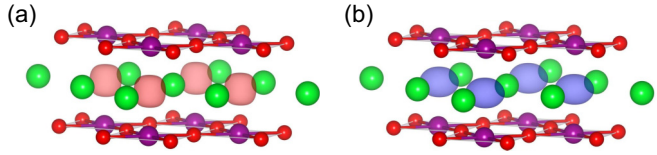

FIG. 4. The squared wave function of (a) spin ↑ and (b) spin ↓ at A point of Brillouin zone slightly above E_F. The isosurface is set to $2.5\times10^{-8}/Å^3$.

A curious question is about the driving force behind this charge order. First of all, the Jahn-Teller instability is excluded since no partially filled degenerate orbitals are found in either spin channel—the degenerate d_{yz} and d_{xz} orbitals of $P4/mmm$ phase are fully occupied (empty) in the spin ↑ (↓) channel despite different values of U (Fig. 6). Instead, we suggest that FSN may play an important role in driving this charge order. In the 1D case, Peierls transition as a consequence of electronic instability and Kohn anomaly results in a simultaneous bond disproportion state and gap opening at E_F. Although the power of FSN in forming charge order decreases with the increasing dimensions [42], $SrMnO_2$ could be approximately decoupled to a quasi-2D spin ↑ channel and a quasi-1D spin ↓ channel, and each part satisfies the corresponding decomposed nesting vector. We illustrate this in two steps. First, we verify that the system can be well decoupled. As shown in Fig. 7, we artificially fixed the vibration of Mn-O bonds in the neighboring Mn-O plane with the same phase (antiphase in the $CmCm$ phase). Only the density of states (DOS) of the spin ↑ channel around E_F is strongly reduced, indicating that the gap opening of the spin ↑ (↓) channel

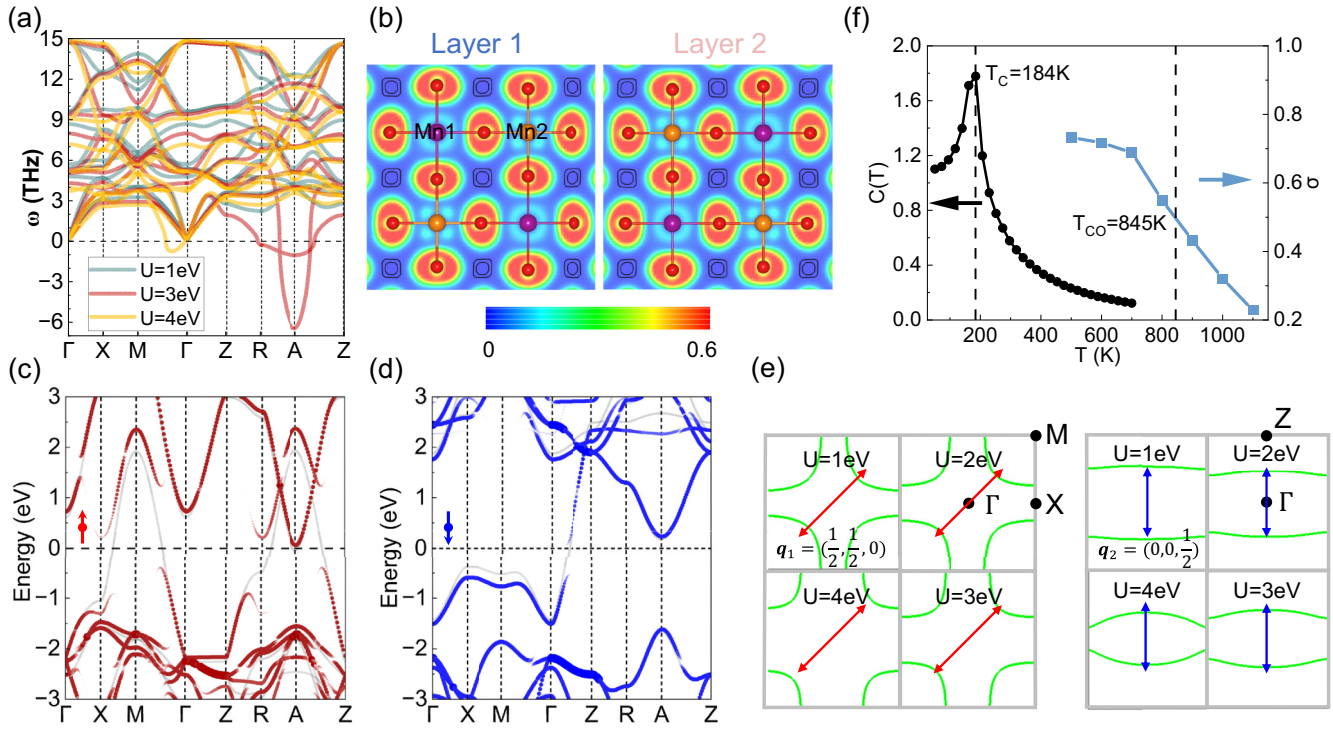

FIG. 5. Electronic properties of charge/bond disproportion phase with $U = 3$ eV. (a) Phonon spectrum of $P4/mmm$ phase under different U within FM configuration. (b) Electron localization function (ELF) of the $CmCm$ phase. Two kinds of Mn with different chemical environments are colored purple and orange, respectively. The number of layers corresponds to Fig. 2(b). (c) Spin ↑ and (d) spin ↓ unfolded band structures of $CmCm$ phase. Band structures of $P4/mmm$ phase are also plotted with gray lines for comparison. (e) Fermi surface sections across Γ point of $P4/mmm$ phase under different U. Left panel: spin ↑ with ab direction. Right panel: spin ↓ with c direction. The proper nesting vector is decomposed into two vectors, which are labeled in the diagram with red and blue arrows. (f) Specific heat $C(T)$ and charge-order parameter σ versus temperature from MC simulation and AIMD, respectively.

is mainly induced by in-plane (out-of-plane) breathing (antiphase) mode. Second, we demonstrate that the nesting condition can be satisfied with decoupled nesting vectors. As shown in Fig. 5(e), the hole pocket of the Fermi surface in the spin ↑ channel shrinks while the Fermi surface of the spin ↓ channel becomes closer to Γ with increasing U. The nesting vector forming such 2×2×2 charge order is $q_{\text{nesting}} = (0.5, 0.5, 0.5)$ reciprocal lattice unit (r.l.u.), which can be decomposed as $q_1 = (0.5, 0.5, 0)$ corresponding to spin ↑ channel and $q_2 = (0, 0, 0.5)$ corresponding to the spin ↓ channel. Overall, the nesting condition can be better satisfied when $U = 2$ and 3 eV than $U = 1$ and 4 eV. Besides, the nesting scenario also agrees with the facts that the collapse in phonon spectra is sharp rather than extended and that the major change of both spin channels is near E_F rather than in the deep valence band [43].

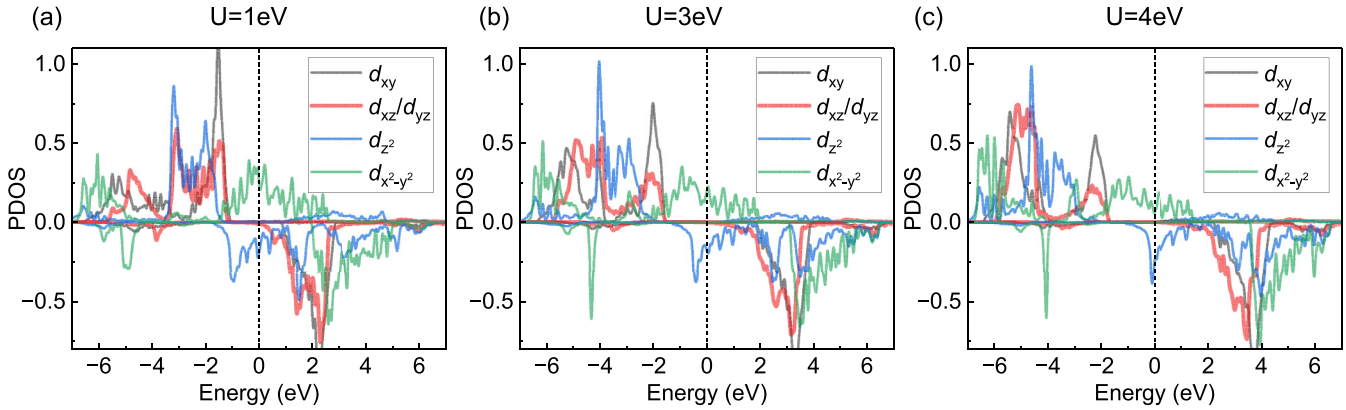

FIG. 6. Projected density of states (PDOS) of the Mn in the $P4/mmm$ $SrMnO_2$ with (a) $U = 1$ eV, (b) $U = 3$ eV, and (c) $U = 4$ eV. PDOS of degenerate d_{xz} and d_{yz} orbitals are thickened.

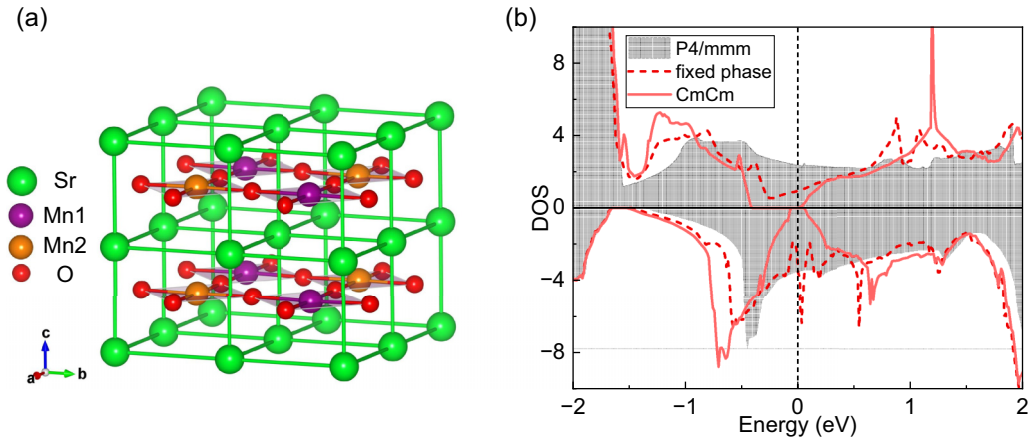

FIG. 7. (a) Structure of artificially fixed $SrMnO_2$. (b) DOS of the artificially fixed structure compared with DOS of $P4/mmm$ and $CmCm$ $SrMnO_2$.

The application of $SrMnO_2$ as a platform to study anomalous Hall effect requires the existence of both charge and FM orders. Thus, it is important to determine the critical temperature of both orders. We performed classic MC simulation on the spin Heisenberg model to obtain Curie temperature T_C and AIMD with the evolution of energy shown in Fig. 8 to obtain the critical temperature of charge order T_{CO}. Here, T_{CO} is approximately determined by $\sigma = 0.5$, where $\sigma(T) = D(T)/D(0)$ and $D(T) = |l_1(T) - l_2(T)|/[l_1(T) + l_2(T)]$ with $l_1(T)$ and $l_2(T)$ are the mean Mn-O bond lengths at temperature T. As shown in Fig. 5(f), while the calculated T_{CO} is ~845 K, the T_C is estimated to be 184 K, lower than the phase without charge order. Remarkably, during the AIMD simulation, FM configuration is set artificially, which disappears above T_C. But the charge order also exists in the ground state despite magnetic orders based on the geometric relaxation. Therefore, it is convincible that $T_C \sim 184$ K is the upper-limit temperature for the coexistence of FM and charge-order state.

Piezoelectricity-switchable AFM orders. $SrMnO_2$ was predicted to be an AFM metal with $U = 5.3$ eV in previous DFT calculations without considering dynamic stabilities [44]. By contrast, in this study, when $U = 5$ eV, despite different magnetic configurations, large structural reconstructions occur, eliminating the charge order and producing nearly degenerate (0.5,0.5,0)/(0.5,0.5,0.5) AFM ground states. As shown in Fig. 9(a), both configurations are insulators with a nearly direct band gap of ~1 eV at the Γ point. However, there are distinct differences between the electronic structures of these two configurations. For example, the valence-band dispersion of the (0.5,0.5,0) configuration around E_F is larger than that of the (0.5,0.5,0.5) configuration. As a consequence, a different response to an external electric field (E_{ext}) is expected. Figure 9(b) shows the energy of different AFM configurations under E_{ext} parallel to the c axis. This suggests that the (0.5,0.5,0) configuration is the ground state when $E_{ext} < 0$ V/Å, the (0.5,0.5,0.5) configuration is the ground state when $0 < E < 0.002$ V/Å, and the (0,0,0.5) configuration is the ground state when $E > 0.003$ V/Å. The magnitude of E_{ext} needed for the magnetic phase transition is quite small (in the order of 10 MV/m) and can be achieved experimentally [45].

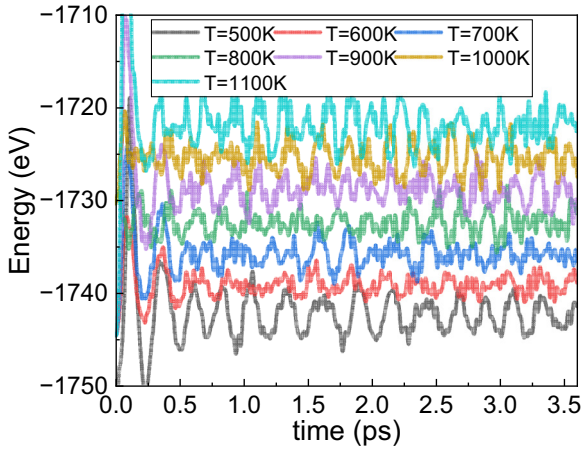

FIG. 8. AIMD simulated energy evolution with time under different temperatures.

On the other hand, emerging piezoelectricity is observed in $P\bar{4}2_1m$ $SrMnO_2$ as a result of noncentric symmetry, which is absent in $P4/mmm$ (small U case) and $CmCm$ (middle U case) phases. The piezoelectric coefficient tensor has two nonzero independent components $e_{14} = e_{25}$ and e_{36}. Unlike an e_{33}, which reflects the polarization change along c due to strain along the same axis (e.g., in $PbZr_xTi_{1-x}O_3$), e_{36} reflects the polarization change along c with response to in-plane strain. As shown in Fig. 9(c), the difference in piezoelectric coefficients of all three AFM configurations is minor ($e_{14} \sim 0.6$ C/m^2 and $e_{36} \sim 1.2$ C/m^2), in agreement with similar structures for different magnetic orders. Besides, since the electric field along c emerges with in-plane strain as a consequence of nonzero e_{36}, the piezoelectric effect may also switch the magnetic ground state. As shown in Fig. 9(d), when a compressive in-plane strain is applied, an electric field along $-c$ is generated, favoring the (0.5,0.5,0) configuration, and when a tensile in-plane strain is applied, the direction of the electric field is reversed, favoring the (0.5,0.5,0.5) configuration. This interesting phenomenon may provide a new idea in

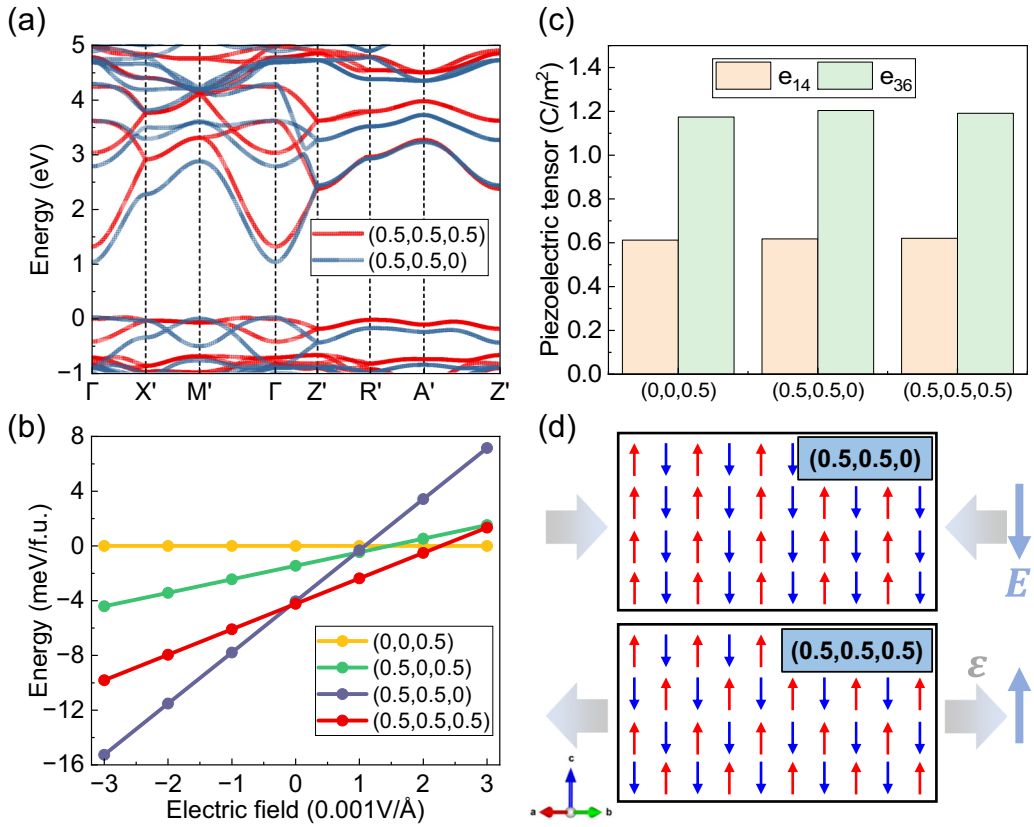

FIG. 9. Electronic properties of nearly degenerate AFM insulating phases with $U = 5$ eV. (a) Band structures of $P\bar{4}2_1m$ phase with (0.5,0.5,0) and (0.5,0.5,0.5) configurations. (b) The energy of AFM configurations under the external electric field. Here the electric field is applied to the c axis. (c) Piezoelectric coefficients of $P\bar{4}2_1m$ phase with (0,0,0.5), (0.5,0.5,0), and (0.5,0.5,0.5) configurations. (d) Schematic diagram of tunable antiferromagnetism by piezoelectricity. Red and blue arrows represent different spin orientations. ε is external strain field and E is the piezoelectricity-induced electric field.

designing a device with AFM order switching by piezoelectricity, a different type of multiferroics.

IV. OUTLOOK AND SUMMARY

The uniqueness of $SrMnO_2$ is observed compared with other infinite-layer systems. While a small change of U (of several eV) does not influence the basic properties of other ABO_2 qualitatively [$SrFeO_2$ (3–6 eV) [22], $CaCoO_2$ (2–6 eV) [16], and $NdNiO_2$ (3–6 eV) [23]], the physical properties of ground-state $SrMnO_2$ is dramatically changed under different U. These properties are highly phase dependent and their existence is associated with the dynamical stability of the phase. Basically, we see that the electronic states around E_F seem to play an important role in determining the dynamical stability. Varying U by several eV would change the FM band splitting dramatically, accompanied by a consequentially changed Fermi surface and Mn-O bonding states of both spin channels. On the other hand, the sensitivity to U indicates that $SrMnO_2$ is indeed on the quantum critical point. Thus, remarkable phase transition can be expected even with a small stimulation. Noticeably, in TMOs, U can be dependent on the local chemical environment and carrier doping. For example, in $PrNiO_2$ [46], U is ∼5 eV while in $LaNiO_2$ [47], U is ∼6 eV by experimental measurements. Once the synthesis of $SrMnO_2$ is realized, the tunability between different phases can be promising through chemical doping or alloying.

Theoretically, the determination of U from first-principles calculations can be insightful. The value of U in infinite-layer $SrMnO_2$, estimated by the DFPT method implemented in QE, is ∼5.4 eV. However, it is worth noting that the accuracy of U estimated with first-principles methods are strongly system dependent [48], often with errors reaching several eV. For example, the U of $SrMnO_3$ by first principles is estimated to be 4.0–4.3 eV [49,50], larger than the empirically used 1.7–3.0 eV [27,28], while for $SrVO_3$, the U by first principles is ∼3.4 eV [51], smaller than the empirical value ∼5 eV [52] used to reproduce experimental spectra features. Therefore, as for $SrMnO_2$, whose property is sensitive to U, experimental measurement may be necessary. Besides, we find that 3% compressive in-plane strain can reduce U by ∼0.3 eV while 3% tensile in-plane strain can increase U by ∼0.6 eV, suggesting that U may be changed by the epitaxial strain of substrates to some degree.

In conclusion, this study unveils unexpected phase transitions in $SrMnO_2$, which is sensitive to the small change of EC. Abundant structural transitions coupled with charge and spin degrees of freedom with novel quantum phenomena are predicted. In the weak EC range, the system is predicted to be ferromagnetic metal with promising application

in spin-valve devices. With the slight increase of EC, the ferromagnetic charge/bond disproportion order occurs related to correlation-driven FSN. When the EC is further enlarged, obvious structural reconstruction into $P\bar{4}2_1m$ symmetry with emergent nearly degenerate AFM orders is predicted, which can be tuned by the electric field induced by the piezoelectricity effect, achieving coupled antiferromagnetic order with polarization. Besides, $A\mathrm{MnO_3}$, as a star material in colossal magnetoresistance effect [53], has played important roles in information storage. Our study would stimulate experimental interest in $\mathrm{SrMnO_2}$ and to check whether its unique properties can be as fascinating as $A\mathrm{MnO_3}$.

ACKNOWLEDGMENTS

This work was supported by the National Key Research and Development of China (Grant No. 2022YFA1402401), NSFC (Grant No. 12088101), and NSAF (Grant No. U2230402). Computations were done at the Tianhe-JK supercomputer at CSRC.

[1] P. Zubko, S. Gariglio, M. Gabay, P. Ghosez, and J.-M. Triscone, Interface physics in complex oxide heterostructures, Annu. Rev. Condens. Matter Phys. **2**, 141 (2011).

[2] D. Xiao, W. Zhu, Y. Ran, N. Nagaosa, and S. Okamoto, Interface engineering of quantum Hall effects in digital transition metal oxide heterostructures, Nat. Commun. **2**, 596 (2011).

[3] Y. Tokura, M. Kawasaki, and N. Nagaosa, Emergent functions of quantum materials, Nat. Phys. **13**, 1056 (2017).

[4] B. Keimer and E. Moore, The physics of quantum materials, Nat. Phys. **13**, 1045 (2017).

[5] R. Ramesh and G. Schlom, Creating emergent phenomena in oxide superlattices, Nat. Rev. Mater. **4**, 257 (2019).

[6] S. Dong, H. Xiang, and E. Dagotto, Magnetoelectricity in multiferroics: A theoretical perspective, Natl. Sci. Rev. **6**, 629 (2019).

[7] C. Ahn, A. Cavalleri, A. Georges, S. Ismail-Beigi, A. J. Millis, and J.-M. Triscone, Designing and controlling the properties of transition metal oxide quantum materials, Nat. Mater. **20**, 1462 (2021).

[8] F. Trier, P. Noël, J.-V. Kim, J.-P. Attan, L. Vila, and M. Bibes, Oxide spin-orbitronics: Spin-charge interconversion and topological spin textures, Nat. Rev. Mater. **7**, 258 (2021).

[9] W. S. Choi, C. M. Rouleau,S. S. A. Seo, Z. Luo, H. Zhou, T. T. Fister, J. A. Eastman, P. H. Fuoss, D. D. Fong, J. Z. Tischler *et al.*, Atomic layer engineering of perovskite oxides for chemically sharp heterointerfaces, Adv. Mater. **24**, 6423 (2012).

[10] Q. Lei, M. Golalikhani, B. A. Davidson, G. Liu, D. G. Schlmo, Q. Qiao,Y. Zhu, R. U. Chandrasena, W. Yang, A. X. Gray *et al.*, Constructing oxide interfaces and heterostructures by atomic layer-by-layer laser molecular beam epitaxy, Npj Quantum Mater. **2**, 10 (2017).

[11] M. G. Smith, A. Manthiram, J. Zhou, J. B. Goodenough, and J. T. Markert, Electron-doped superconductivity at 40 K in the infinite-layer compound Sr1-yNdyCuO2, Nature (London) **351**, 549 (1991).

[12] M. Azuma, Z. Hiroi, M. Takano, Y. Bando, and Y. Takeda, Superconductivity at 110 K in the infinite-layer compound $(\mathrm{Sr}_{1-x}\mathrm{Ca}_x)_{1-y}\mathrm{CuO_2}$, Nature (London) **356**, 775 (1992).

[13] D. Li, K. Lee, B. Y. Wang, M. Osada, S. Crossley, H. R. Lee, Y. Cui, Y. Hikita, and H. Y. Hwang, Superconductivity in an infinite-layer nickelate, Nature (London) **572**, 624 (2019).

[14] Y. Tsujimoto, C. Tassel, N. Hayashi, T. Watanabe, H. Kageyama, K. Yoshimura, M. Takano, M. Ceretti, C. Ritter, and W. Paulus, Infinite-layer iron oxide with a square-planar coordination, Nature (London) **450**, 1062 (2007).

[15] C. Tassel, T. Watanabe, Y. Tsujimoto, N. Hayashi, A. Kitada, Y. Sumida, T. Yamamoto, H. Kageyama, M. Takano, and K. Yoshimura, Stability of the infinite layer structure with iron square planar coordination, J. Am. Chem. Soc. **130**, 3764 (2008).

[16] W. J. Kim, M. A. Smeaton, C. Jia, B. H. Goodge, B.-G. Cho, K. Lee, M. Osada, D. Jost, A. V. Ievlev, B. Moritz *et al.*, Geometric frustration of Jahn-Teller order in the infinite-layer lattice, Nature (London) **615**, 237 (2023).

[17] B. Keimer, S. A. Kivelson, M. R. Norman, S. Uchida, and J. Zaanen, From quantum matter to high-temperature superconductivity in copper oxides, Nature (London) **518**, 179 (2015).

[18] S. Paschen and Q. Si, Quantum phases driven by strong correlations, Nat. Rev. Phys. **3**, 9 (2020).

[19] V. I. Anisimov, J. Zaanen, and O. K. Andersen, Band theory and Mott insulators: Hubbard U instead of Stoner I, Phys. Rev. B **44**, 943 (1991).

[20] V. I. Anisimov, F. Aryasetiawan, and A. I. Lichtenstein, First-principles calculations of the electronic structure and spectra of strongly correlated systems: The LDA + U method, J. Phys.: Condens. Matter **9**, 767 (1997).

[21] S. L. Dudarev, G. A. Botton, S. Y. Savrasov, C. J. Humphreys, and A. P. Sutton, Electron-energy-loss spectra and the structural stability of nickel oxide: An LSDA + U study, Phys. Rev. B **57**, 1505 (1998).

[22] H. J. Xiang, S.-H. Wei, and M.-H. Whangbo, Origin of the Structural and Magnetic Anomalies of the Layered Compound $\mathrm{SrFeO_2}$: A Density Functional Investigation, Phys. Rev. Lett. **100**, 167207 (2008).

[23] E. Been, W.-S. Lee, H. Y. Hwang, Y. Cui, J. Zaanen, T. Devereaux, B. Moritz, and C. Jia, Electronic Structure Trends Across the Rare-Earth Series in Superconducting Infinite-Layer Nickelates, Phys. Rev. X **11**, 011050 (2021).

[24] G. Kresse and J. Furthmüller, Efficient iterative schemes for ab initio total-energy calculations using a plane-wave basis set, Phys. Rev. B **54**, 11169 (1996).

[25] P. E. Blöchl, Projector augmented-wave method, Phys. Rev. B **50**, 17953 (1994).

[26] J. P. Perdew, K. Burke, and M. Ernzerhof, Generalized Gradient Approximation Made Simple, Phys. Rev. Lett. **77**, 3865 (1996).

[27] J. H. Lee and K. M. Rabe, Epitaxial-strain-induced Multiferroicity in SrMnO3 from First Principles, Phys. Rev. Lett. **104**, 207204 (2010).

[28] A. Edström and C. Ederer, First-principles-based strain and temperature-dependent ferroic phase diagram of $SrMnO_3$, Phys. Rev. Mater. **2**, 104409 (2018).
[29] M. Kawamura, FermiSurfer: Fermi-surface viewer providing multiple representation schemes, Comput. Phys. Commun. **239**, 197 (2019).
[30] P. V. C. Medeiros, S. Stafström, and J. Björk, Effects of extrinsic and intrinsic perturbations on the electronic structure of graphene: Retaining an effective primitive cell band structure by band unfolding, Phys. Rev. B **89**, 041407 (2014).
[31] P. V. C. Medeiros, S. S. Tsirkin, S. Stafström, and J. Björk, Unfolding spinor wave functions and expectation values of general operators: Introducing the unfolding-density operator, Phys. Rev. B **91**, 041116 (2015).
[32] A. Togo and I. Tanaka, First principles phonon calculations in materials science, Scr. Mater. **108**, 1 (2015).
[33] L. Liu, X. Ren, J. Xie, B. Cheng, W. Liu, T. An, H. Qin, and J. Hu, Magnetic switches via electric field in BN nanoribbons, Appl. Surf. Sci. **480**, 300 (2019).
[34] S. Nosé, A unified formulation of the constant temperature molecular dynamics methods, J. Chem. Phys. **81**, 511 (1984).
[35] W. G. Hoover, Canonical dynamics: Equilibrium phase-space distributions, Phys. Rev. A **31**, 1695 (1985).
[36] I. Timrov, N. Marzari, and M. Cococcioni, Hubbard parameters from density-functional perturbation theory, Phys. Rev. B **98**, 085127 (2018).
[37] I. Timrov, N. Marzari, and M. Cococcioni, Self-consistent Hubbard parameters from density-functional perturbation theory in the ultrasoft and projector-augmented wave formulations, Phys. Rev. B **103**, 045141 (2021).
[38] P. Giannozzi, S. Baroni, N. Bonini, M. Calandra, R. Car, C. Cavazzoni, D. Ceresoli, G. L. Chiarotti, M. Cococcioni, I. Dabo *et al.*, QUANTUM ESPRESSO: A modular and open-source software project for quantum simulations of materials, J. Phys.: Condens. Matter **21**, 395502 (2009).
[39] A. S. Botana and M. R. Norman, Similarities and Differences between $LaNiO_2$ and $CaCuO_2$ and Implications for Superconductivity, Phys. Rev. X **10**, 011024 (2020).
[40] Y. Nomura and R. Arita, Superconductivity in infinite-layer nickelates, Rep. Prog. Phys. **85**, 052501 (2022).
[41] S. D. Bader and S. S. P. Parkin, Spintronics, Annu. Rev. Condens. Matter Phys. **1**, 71 (2010).
[42] M. D. Johannes and I. I. Mazin, Fermi surface nesting and the origin of charge density waves in metals, Phys. Rev. B **77**, 165135 (2008).
[43] K. Rossnagel, On the origin of charge-density waves in select layered transition-metal dichalcogenides, J. Phys.: Condens. Matter **23**, 213001 (2011).
[44] M. Rahman, K.-C. Zhou, Y.-Z. Nie, and G.-H. Guo, Electronic structure and magnetism of layered compounds $SrBO_2$ (B = Ni, Co, Mn): A theoretical investigation, Solid State Commun. **266**, 6 (2017).
[45] T. Lottermoser, T. Lonkai, U. Amann, D. Hohlwein, J. Ihringer, and M. Fiebig, Magnetic phase control by an electric field, Nature (London) **430**, 541 (2004).
[46] Z. Chen, M. Osada, D. Li, E. M. Been, S.-D. Chen, M. Hashimoto, D. Lu, S.-K. Mo, K. Lee, B. Y. Wang *et al.*, Electronic structure of superconducting nickelates probed by resonant photoemission spectroscopy, Matter **5**, 1806 (2022).
[47] M. Hepting, D. Li, C. J. Jia, H. Lu, E. Paris, Y. Tseng, X. Feng, M. Osada, E. Been, Y. Hikita *et al.*, Electronic structure of the parent compound of superconducting infinite-layer nickelates, Nat. Mater. **19**, 381 (2020).
[48] R. Tesch and P. M. Kowalski, Hubbard U parameters for transition metals from first principles, Phys. Rev. B **105**, 195153 (2022).
[49] L. Vaugier, H. Jiang, and S. Biermann, Hubbard U and Hund exchange J in transition metal oxides: Screening versus localization trends from constrained random phase approximation, Phys. Rev. B **86**, 165105 (2012).
[50] C. Ricca, I. Timrov, M. Cococcioni, N. Marzari, and U. Aschauer, Self-consistent site-dependent DFT + U study of stoichiometric and defective $SrMnO_3$, Phys. Rev. B **99**, 094102 (2019).
[51] Y. Nomura, M. Kaltak, K. Nakamura, C. Taranto, S. Sakai, A. Toschi, R. Arita, K. Held, G. Kresse, and M. Imada, Effective on-site interaction for dynamical mean-field theory, Phys. Rev. B **86**, 085117 (2012).
[52] E. Pavarini, S. Biermann, A. Poteryaev, A. I. Lichtenstein, A. Georges, and O. K. Andersen, Mott Transition and Suppression of Orbital Fluctuations in Orthorhombic $3d^1$ Perovskites, Phys. Rev. Lett. **92**, 176403 (2004).
[53] A. P. Ramirez, Colossal magnetoresistance, J. Phys.: Condens. Matter **9**, 8171 (1997).